Korean J. Chem. Eng., 38(7), 1469-1486 (2021)
DOI: 10.1007/s11814-021-0777-5

pISSN: 0256-1115
eISSN: 1975-7220

Preparation of alumina nanotubes for incorporation into CO_2 permselective Pebax-based nanocomposite membranes

Nikoo Soltani and Omid Bakhtiari†

Membrane Research Center, Faculty of Petroleum and Chemical Engineering, Razi University, Kermanshah, Iran
(*Received 17 April 2020 • Revised 15 February 2021 • Accepted 7 March 2021*)

Abstract−Nanocomposite membranes were prepared using Pebax 1657, glycerol triacetate (GTA), and alumina nanotubes (ANTs) by solution casting method. Hydrothermally synthesized ANTs were characterized using SEM, FTIR, and XRD, and additional analysis of FESEM and DSC was also performed on the prepared membranes. ANTs loadings and employed solvent type, dimethylformamide (DMF) or ethanol/water mixture, impacts were investigated on CO_2 permeability and ideal CO_2/CH_4 selectivity of the nanocomposite membranes. CO_2 permeability of the ANTs - Pebax nanocomposite membranes was improved compared with the neat Pebax membrane. In the 4 wt% ANTs loaded nanocomposite membrane, chain packing and fractional free volume of its polymeric matrix were tuned by GTA addition (10-40 wt%) to improve the penetrants' permeability through. The Pebax membrane loaded by 4 and 40 wt% of ANTs and GTA revealed 73.75 and −4.97% changes in its CO_2 permeability and ideal CO_2/CH_4 selectivity, respectively. Successful ANTs functionalization by 3-aminopropyltriethoxysilane agent (FC-ANTs), for their higher compatibility with the polymeric chains, was confirmed using FTIR analysis. 2 wt% FC-ANTs loaded nanocomposite membranes' ideal selectivity prepared by using DMF and ethanol/water mixture solvents improved by 5.71 and 14.7%, respectively, while their CO_2 permeability decreased by 11.95 and 11.8%.

Keywords: Pebax, Aminosilane Grafting, Glycerol Triacetate, Nanocomposite Membrane, CO_2/CH_4 Separation

INTRODUCTION

Raw natural gas mainly consists of methane and some other light gases/impurities like CO_2, H_2O, C_2H_6, C_3H_8, and H_2S with a composition varying over its field and recovery time. The natural gas impurities have devastating effects, such as equipment and pipeline corrosion and also reduction of gas heating value and its conducting pipeline transfer capacity [1]. Removal of water vapor, acid gases (i.e., gas sweetening), and heavier hydrocarbons are crucial steps for natural gas to meet transportation and final usage requirements as different industries feed/fuel consumption. There are various gas separation processes, such as pressure swing adsorption (PSA), physical and chemical absorption by amine solutions, cryogenic distillation, and membranes [2], which are used for these tasks. Among the various natural gas sweetening processes, polymer-based membrane technology is classified as the most reliable compared with the other processes due to its outstanding advantages such as mechanical strength and higher flexibility, thermal stability, lower capital and operating costs, modular design, and simple operation and maintenance [3]. However, based on the Robeson upper bound limit [4], current polymeric membranes are limited in an intrinsic trade-off between their permeability and selectivity. On of the major approaches to overcome this limitation is incorporation of different kinds of inorganic and organic filler particles as dispersed phase known as mixed matrix membranes (MMMs), which are expected to have superior separation performance compared with the pristine polymeric membrane [5].

One of the most important key factors in the membrane preparation process is its material(s) selection [6]. It seems that utilizing polymers with low glass transition temperatures (T_g) in mixed matrix/nanocomposite membranes' preparation is more attractive than those with high T_g values due to the prepared almost all defect-free membranes. Also, utilizing copolymers as the basic polymer materials for the membrane preparation goes back to many years ago [6]. Polyether block amide as a multi-block copolymer and a thermoplastic elastomer, which is known as Pebax in the market, contains flexible linear chains of polyether (PE) having large free volume as soft permeable rubbery segments and hard aliphatic polyamide (PA6) segments with selective nature. The amorphous chains of polyether linkages in the polymer matrix provide better affinity towards polar gas molecule penetrants such as CO_2 over non-polar gas molecules like CH_4 while its hard crystalline (glassy) polyamide supplies the polymer's mechanical strength acts as the membrane [7,8].

Numerous surveys have been performed to modify the polymeric membranes separation performance via two types of porous [9,10] and nonporous [11] inorganic filler particles incorporation as dispersed phase for MMMs prepearation. Typical kinds of nonporous (impermeable) inorganic filler particles are metal oxides [12] like TiO_2 [11,13], silica [14,15], fullerene (C60) [16] and common prominent porous materials applied as dispersed phase are carbon molecular sieves [17], carbon nanotubes (CNTs) and MWCNT [18], graphene oxide (GO) [19], mesoporous silicas [20,21], zeolites [22,23], zeolitic imidazolate frameworks (ZIFs) [24], metal-organic frameworks (MOFs) [25,26] are the most popular incorporated filler particles in the polymeric phase, including rubbery

†To whom correspondence should be addressed.
E-mail: obakhtiari@razi.ac.ir
Copyright by The Korean Institute of Chemical Engineers.

and glassy polymers. The particles incorporation also disrupts chain packing of the polymer matrix and enhances their free fractional volume (FFV) [27]; in addition, their intrinsict superior separation characteristcs potentially boost the resultant membrane separation performance.

After approving outstanding properties of carbon nanotubes', i.e., their high surface area and mechanical and mass transfer properties, many researchers were encouraged to prepare other inorganic materials one-dimensional nanostructured from such as metallic oxides nanotubes. These nanotubes' unique properties like low density, hollow structure, specific shape and quantum-size effect made them interesting for different applications, such as drug delivery systems [28], solar cells [29], electrical and optical sensors [30], and efficient filler particles for incorporation in polymer membranes [31]. For instance, titanium dioxide (TiO_2) nanotubes have numerous applications in photocatalysis [32], solar cells [33], electrochromic devices [34], and gas sensors [35]. Song et al. prepared TiO_2 nanotubes by hydrothermal method and impregnated them by various amines of ethylenediamine (ED), polyetherimide (PEA), and tetraethylenepentamine (TEPA) and evaluated them for CO_2 adsorption. They reported that the as-synthesized nanotubes have large surface area of 302.7 m^2/g and adsorption capacity of 40.48 mg CO_2/g, while the TEPA modified TiO_2 nanotubes revealed the highest adsorption capacity as 167.64 mg CO_2/g [36].

Aluminum oxide (Al_2O_3), as one of the most common inorganic materials, is used in many applications due to its especial characteristics like elevated melting temperature, high thermal stability, large elastic modulus, hydrophilic nature, low surface acidity, and available inexpensive material. γ-Al_2O_3 is the alumina crystalline phase which is widely applied as catalyst supports in the petroleum industries [37]. Baltrusaitis et al. investigated CO_2 adsorption on the 13 nm γ-Al_2O_3 nanoparticles surface using infrared spectroscopy at 296 K and 0.274 torr. They recorded transmission spectra before and after the nanoparticles' CO_2 exposure at constant pressure and monitored the CO_2 uptake was over time. The initial adsorption rate within the first 50-100 s after CO_2 gas introduction into the adsorption cell was found as 0.0022 s^{-1} [38]. Cheng et al. used the sol-gel process to prepare mesoporous alumina with high surface area (812 m^2/g) and large pore volume (0.83 cm^3/g) and reported 52 and 381 mg CO_2/g adsorbent at 25 °C and 1 and 30 bar, respectively, while finding those for commercial γ-alumina as 30 and 259 mg CO_2/g adsorbent. Afterward, they impregnated the synthesized mesoporous alumina using polyethyleneimine (PEI) and found their CO_2 uptake at 75 °C and 1 atm as 120 mg CO_2/g adsorbent during five consecutive adsorption and desorption cycles [39]. Herein, the alumina CO_2 adsorption capacity and characteristics of metal oxides nanotubes together led to idea of alumina nanotube synthesis as potentially great filler particles for nanocomposite CO_2 permeable membranes.

Silane coupling (grafting) agent formula is $RnSiX_4$-n formula, which its functional organic (such as amino) and hydrolyzable inorganic reactive (such as methoxy, ethoxy, or acetoxy) groups are indicated by R and X, respectively [40]. These silicon-based chemicals groups can readily react with the filler particles surficial hydroxyl groups besides the polymer chains amino/functional groups to improve their interfacial affinity [41]. Then, silane modified surface nanoparticles have higher adhesivity toward their incorporated polymer matrix chains used for nanocomposite membranes preparation. Ameri et al. employed alumina nanoparticles for polyurethane (PU) nanocomposite membrane preparation. They used two different chain extenders of 2-methyl-1, 3-propanediol and 1,4-butane-diol in the linear polymer synthesis. Their results showed that as the alumina loading increases from 0 to 30 wt%, the nanocomposite membranes' CO_2/N_2, CO_2/CH_4, and O_2/N_2 selectivity enhances by 1.5, 1.87 and 0.27 times, respectively, while MPD-based PU CO_2 permeability decreases by 38% [42]. Pechar et al. incorporated aminopropyl-triethoxysilane (APTES) silanized zeolite L into polyimide matrix of 6FDA-6FpDA-DABA. Compared with the pristine polymeric membrane, both CO_2 permeability and CO_2/CH_4 selectivity of the 20 wt% loaded amine-functionalized zeolites nanocomposite membrane at 4 atm transmembrane pressure dropped by 4.7 and 18.36%, respectively. They attributed the reductions to gas molecules restricted access to the zeolite partially blocked pores by APTES [43]. Laghaei et al. prepared MMMs using polyethersulfone (PES) and mesoporous silica (MCM-41) filler particles modified by APTMS and TMCS silane coupling agents. Gas permeation rates through the polymeric membranes at 8 bar and ambient temperature increased as the raw and silanized MCM-41 particles were incorporated. The CO_2 permeability of 20 wt% loaded raw, APTMS-modified and TMCS-modified MCM-41 was enhanced by 1.54 times, 74.6 and 52.8%, respectively. They found that formation of non-ideal interfacial voids after incorporation of raw MCM-41 resulted in decrement of O_2/N_2 selectivity from 5.1 for pure PES membrane to 4.2 for 20 wt% loaded PES-MCM-41 nanocomposite membrane. However, after APTMS silanation of MCM-41, the polar groups on the filler particles resulted in their good compatibility with the continuous phase and preparaion of defect-free nanocomposite membranes. Therefore, their gas pairs selectivity for O_2/N_2 and CO_2/CH_4 increased by 9.8 and 39%, respectively, at the modified nanoparticle loading of 20 wt%. The nonpolar TMCS groups where replaced with OH groups hinder appropriate interaction between the filler particles resulting in their agglomeration at their higher loadings. Hence, the O_2/N_2 and the CO_2/CH_4 selectivity was increased by 37.25% and 19.1% at 5 wt% of the particles. However, O_2/N_2 and CO_2/N_2 selectivity declined for the filler loadings higher than 5 wt%, as they were reduced by 22.8 and 14.61% from 7 and 26 to 5.4 and 22.2, respectivley, and CO_2/CH_4 selectivity declined from 30.5 for 5 wt% to 25.9 for 20 wt% attributed to the particles poor interfacial adhesion and agglomeration [44].

A variety of studies have been applied to add ethylene oxide groups including polyethylene glycol (PEG) or ionic liquid into the polymeric matrix to decrease particle-polymer interface incompatibility. For instance, Jomekian et al. used a synthesized ionic liquid of DnBMCl and filler particles of ZIF-8 to modify Pebax1657 membrane and found improved polymer - filler particle interactions led to enhancing both the membrane permeability and ideal selectivity of CO_2/CH_4, CO_2/N_2, CO_2/H_2 gas pairs over those of the pristine polymeric membrane [45]. Shoafi et al. added low and high molecular weight PEGs into matrix of multi-walled carbon nanotubes (MWCNTs) - Pebax MMMs. They observed that addition of low molecular weight PEG-based polymer (PEGDME) has

a desirable effect on the CO_2/N_2 separation performance, while addition of high molecular weight PEG (PEG20000) was favorable for CO_2/CH_4 separation [46].

Glycerol triacetate (GTA), a CO_2-philic low molecular weight material contains acetate groups with strong CO_2 affinity, was added to polymer matrixes and acted as a plasticizer, i.e., made the membrane more flexible and gel-like [47]. Rabiee et al. showed that GTA addition to the polymer matrix enhanced the gaseous penetrants' permeation rates by increasing their diffusivity. Even though CO_2/CH_4 and CO_2/N_2 selectivity decreased slightly as the GTA added while CO_2/H_2 selectivity was enhanced by two times. Furthermore, the resultant GTA added gel membranes' separation performance for CO_2/N_2 feed passed over the 2008 Robeson upper bound limit. They reported that the 80 wt% GTA loaded membrane permeability at 4 bar and room temperature enhanced by eight times via the CO_2 solubility increment, while its CO_2/CH_4 selectivity decreased by 59% [48].

Auta and Hameed [49] and also Esmaili and Ehsani [50] reported attractive CO_2 adsorption properties of alumina, and Tena et al. [51] employed alumina particles as filler within MMMs. The pointed out enhanced properties of tubular form of TiO_2 and carbon over those of their particulate form, along with our best knowledge which there was no study on CO_2 adsorption capacity of nanotubular shaped alumina, encouraged us to prepare functionalized tubular form of alumina for incorporating and improving neat Pebax membrane CO_2 permeation properties. Pebax, as a popular family of copolymers, has been employed as membrane matrix in many studies [45,46] and we also found proper film forming and also separation properties of Pebax 1657 in our previous studies [52,53].

In this study, first, alumina nanotubes (ANTs) were synthesized by the hydrothermal method. The ANTs were characterized using Fourier transform infrared (FTIR), X-ray diffraction analysis (XRD), scanning electron microscopy (SEM). Then, the nanotubes surfaces were grafted with APTES (FC-ANTs) and different loadings of ANTs and FC-ANTs (0-10 wt%) were incorporated into the Pebax-1657 matrix using two solvents of N, N-Dimethylformamide (DMF) and 70/30 mixture of ethanol/water. The novel nanocomposite membranes were characterized by field emission scanning electron microscopy (FESEM) and differential scanning calorimetry (DSC). Eventually, the Pebax/4 wt% ANTs nanocomposite membrane was further modified by addition of 0-40 wt% GTA and evaluated for CO_2 and CH_4 permeation.

EXPERIMENTAL

1. Materials

Arkema product of Pebax 1657 was purchased, aluminium nitrate nonahydrate ($Al(NO_3)_3{\cdot}9H_2O$), N-Cetyl-N, N, N-trimethyl ammonium bromide (CTAB, $C_{16}H_{33}N(CH_3)_3Br$), urea ($CO(NH_2)_2$), 3-Aminopropyltriethoxysilane (APTES), N, N-dimethylformamide (DMF), ethanol and glycerol triacetate (GTA) were received from Merck Co. CO_2 and CH_4 (purity of 99.99 and 99.95%, respectively) gases were provided by Tehran Farafan Gas Company, Tehran,

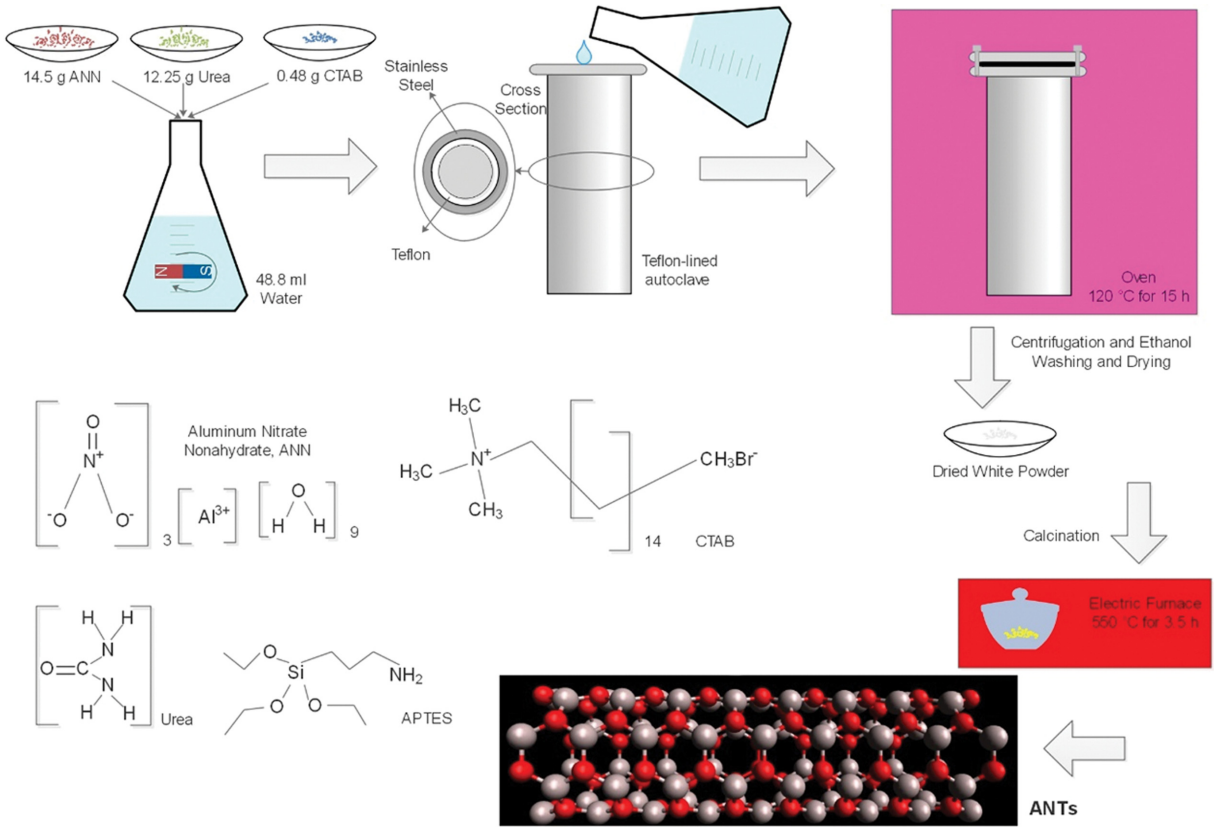


Fig. 1. Schematic representation of ANTs preparation procedure.

Iran. All the received materials were used without any treatment.

2. Alumina Nanotubes (ANTs) Synthesis

Alumina nanotubes were synthesized by a hydrothermal method as previously reported by Dahlan et al. [54]. First, 14.5 g of aluminum nitrate nonahydrate, as a precursor, 12.25 g of urea, and 0.48 g CTAB, as a surfactant, were dissolved in 48.8 ml of deionized water under magnetic stirring to finally obtain a transparent solution. Secondly, the solution was poured into a Teflon-lined autoclave (made from stainless steel and has effective volume of 100 ml), and heated to 125 °C for 15 h. After naturally cooling the autoclave to room temperature, white powder particles were collected by centrifuging its content and washed by ethanol for several times. The obtained white product was desiccated at 120 °C for 12 h and then calcined at 550 °C inside an electric furnace for 3.5 h. Schematic representation of ANTs preparation procedure is shown schematically in Fig. 1. Note that ANTs molecular structure is inspired from Kim et al. [55].

3. Surface Grafting of ANTs with Aminosilane (Amine Functionalization)

APTES grafting of ANTs was carried out based on a procedure reported by Soroush et al. with a little modification in pH of the grafting medium [56]. First, the synthesized ANTs (0.5 g) were dispersed in ethanol (20 mL) for 15 min under continuous sonication. Then, the obtained mixture was stirred in a pH neutral medium at 80 °C for 1 h, and after that a few drops of acetic acid were added for acidification and O-H groups addition. Next, 2 ml APTES was added drop by drop to the mixture in a time duration of 30 min while keeping it stirred. The chemical reaction continued for 24 h, and after that the mixture was naturally cooled to room temperature. For removal of remaining unreacted modification agent (if any) from the obtained mixture, the modified ANTs were collected by centrifugation and then dispersed in fresh ethanol for several times. The last product collected by centrifugation was dried at 100 °C inside an evacuated oven for 24 h.

4. Preparation of the Pristine and the Nanocomposite Membranes

8 wt% solutions of Pebax 1657 were in two separate solvents of DMF and EtOH/Water mixture 70/30 by weight. The solution casting method was employed for preparation of both the pristine and the nanocomposite membranes followed by solvent evaporation. For preparation of pristine membranes, prescribed amount of Pebax-1657 granules was dissolved in different solvents of DMF at 120 °C for 3 h or EtOH/water mixture at 80 °C for 4 h under reflux and magnetic stirring. A flask containing the stirring solution was placed in an oil bath. Next, the prepared solutions were cast on glass Petri dishes and warmed to 65 °C inside an oven and kept for 10 h. Then, the dried membrane films were peeled off by aid of n-hexane. To completely remove the residual solvent(s), the prepared films were desiccated at 60 °C in an evacuated oven for a day.

For the nanocomposite membrane preparation, different amounts of synthesized and grafted ANTs were dispersed in the solvents of DMF or a mixture of EtOH/water under ultrasound waves (Hielscher, UP400S probe sonicator) for 15 min. Following this,

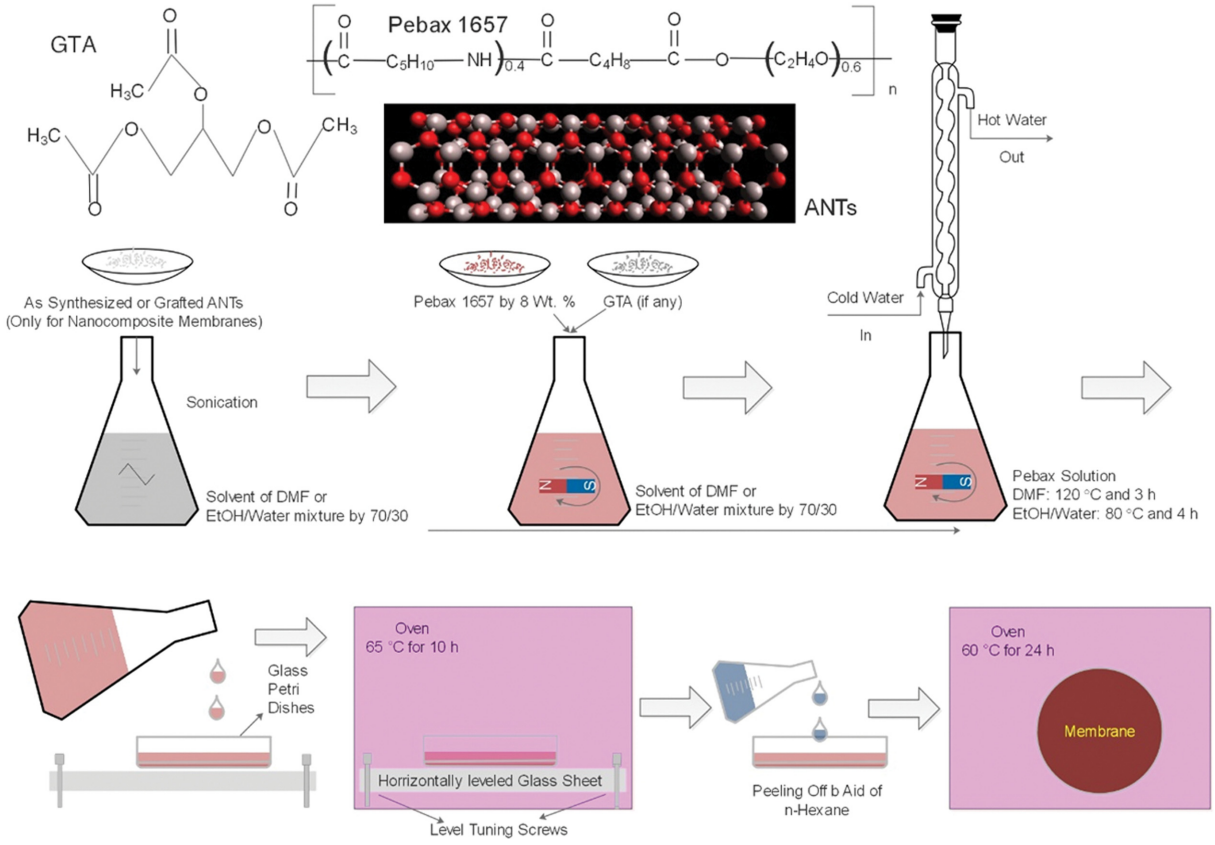


Fig. 2. Schematic of different membrane preparation procedure.

the polymer granules were also dissolved in the solvent and the ultimate suspension was kept in an oil bath under condition as same as the preparation of the pristine membrane. The similar casting and drying procedures, introduced previously for the pristine membranes, were also applied on the nanocomposite membranes.

To prepare the Pebax/GTA/ANTs nanocomposite membranes, the Pebax/ANTs mass ratio was fixed on 8 : 4 since higher concentrations of polymer resulted in thicker films with lower permeability. The 4 wt% of ANTs loaded nanocomposite membranes almost had the same selectivity as the pristine polymeric membranes. On the hand, the selectivity of the nanocomposite membranes with higher ANTs loadings prepared using DMF solvent decreased by 7.25%.

The prepared membranes with EtOH/Water and GTA were not quite homogeneous after solvent evaporation since GTA is little soluble in water [48]. First, various amounts of GTA were dissolved in DMF at ambient temperature for 0.5 h, and then the specified amount of ANTs was added to the solution. Ultrasonication was employed for homogenization of the resultant mixture for 20 min, and ultimately polymer granules were dissolved in the solution under vigorous stirring and reflux at 120 °C for 3 h. Finally, the cast dried membrane films were peeled off and dried in the same way described above for the pristine membranes. The neat and the nanocomposite membrane preparation procedure is shown schematically in Fig. 2.

5. Characterization Techniques

A digital micrometer (accuracy of ±1 μm) was employed to measure thickness of each prepared membrane in different several points and their average value was recorded as its thickness. The membrane thickness was found in the range of 80-100 μm. Morphology and true synthesis of ANTs were checked by a field emission scanning electron microscope (FESEM, MIRA III/TESCAN) and scanning electron microscope (SEM, model AIS2300-seron Technologies, Korea, High-tech Lab.). Morphology of the Pebax/4 wt% ANTs and the Pebax/4 wt% ANTs/20 wt% GTA nanocomposite membranes was also characterized by the FESEM. Glass transition temperature (T_g) and melting point (T_m) of the neat polymeric/Pebax/4 wt% ANTs/20 wt% nanocomposite membranes were detemined using differential scanning calorimetry (DSC, MAHAMAX platform) at 10 °C/min of heating rate from - 80 to 250 °C in the nitrogen environment.

For investigating the grafted ANTs functional groups and evaluation of occurred changes through the prepared membrane modification, Fourier-transform-infrared (FTIR) spectroscopy was employed by using BRUKER Vertex 70FTIR spectrometer in scan range of 600-4,000 cm^{-1} and resolution of 2 cm^{-1}. The samples' X-ray diffraction (XRD) patterns were gathered using the XPERT-MPD apparatus in a 2θ range of 10-90° and scanning rate of 0.2° s^{-1}. The average *d*-spacing of the membranes was calculated by the Bragg's law as given by the following Equation [57]:

$$d = \frac{n\lambda}{2\sin\theta} \quad (1)$$

where d is the structure's d-spacing, n is a positive integer, λ is the incident wavelength and θ is the scattering angle.

6. Gas Permeation Measurement Setup

There are two usual methods to measure gaseous permeability through a membrane including constant volume and constant pressure. In this study, the pure gaseous penetrant permeability through the membranes was evaluated by the constant volume - variable pressure method. Fig. 3 represents a schematical diagram of the employed gas permeation measurement set-up. The operating temperature of the membrane module was kept constant by placing it inside a well-controlled temperature oven. A pressure regulator was employed to easily adjust the transmembrane pressure. All of the experiments were carried out at constant operating temperature and pressure of 35 °C and 5 bar, respectively. A

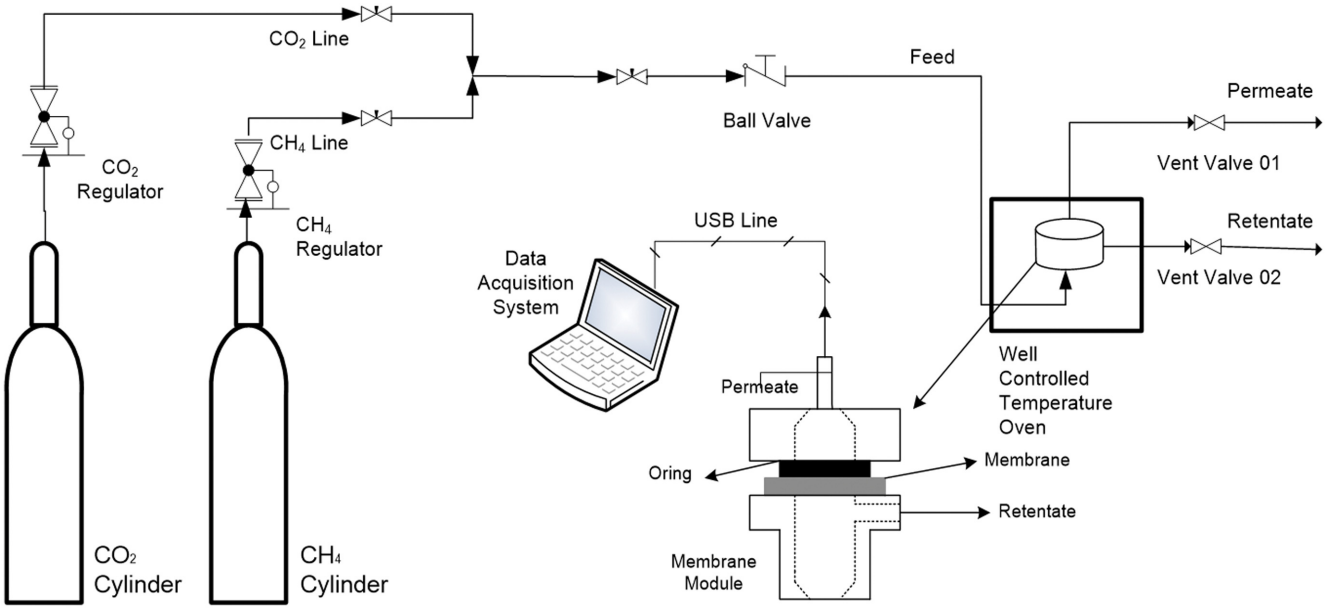


Fig. 3. Schematic presentation of the membrane module and the Lab-scale setup used for measurement of the gaseous penetrants permeabilities.

gaseous penetrant permeability under steady-state condition was calculated using Eq. (2) [58]:

$$P = \frac{1}{p_s}\frac{T_s}{T}\frac{V}{A}\frac{l}{\Delta p}\frac{dp}{dt} \quad (2)$$

where P is the gaseous penetrant permeability through the membrane (10^{-10} cm^3 (STP)·cm/(cm^2·s·cmHg), known as Barrer), V is the membrane permeate (downstream) side's volume (cm^3), A is the membrane active area (23.758 cm^2), T is the operating temperature (K), T_s and p_s are standard temperature (273.15 K) and pressure (76 cmHg), respectively, Δp is the transmembrane pressure (mmHg), dp/dt represents steady-state permeate pressure increment rate (cmHg/s), and *l* is the membrane thickness (cm).

Ideal CO_2/CH_4 selectivity (α_{CO_2/CH_4}) of the prepared membranes was calculated by dividing their CO_2 over their CH_4 permeability using the following equation [58]:

$$\alpha_{CO_2/CH_4} = P_{CO_2}/P_{CH_4} \quad (3)$$

7. Gas Adsorption Measurement Setup

The gaseous CO_2 and CH_4 adsorption on the synthesized nanotubes and grafted alumina nanotubes were measured experimentally at room temperature. The employed constant dual-volume adsorption setup by pressure decay method, as is schematically shown in Fig. 4, was used for adsorption measurement. For each experiment, 0.1 g of the adsorbent particles was placed in a closed and constant volume (270 cm^3) adsorption cell. The feed gas at the first entered to a reference cell volume, which was interconnected to the sample cell. The cells were evacuated using a vacuum pump and then charged stepwise with the desired gas while its pressure change over time was recorded. After reaching pressure equilibrium at each step (i.e., no further pressure decay over time), the next pressure pulse was applied up to ultimate pressure of 7 bar. Changes in the gas mole numbers in the reference/sample cells were calculated by using the Peng-Robinson equation of state [59,60] and then the balances were attributed to the particle adsorption capacity in terms of kmol of adsorbed gas per kg of adsorbent.

The Langmuir adsorption isotherm equation was found as a proper model for fitting on the gathered gas adsorption data as the following Equation [61]:

$$q_e = \frac{q_m b p_e}{1 + b p_e} \quad (4)$$

The model parameters were determined using its following linearized form and the least square method [61]:

$$\frac{p_e}{q_e} = \frac{p_e}{q_m} + \frac{1}{b q_m} \quad (5)$$

where q_e and q_m (one of the model parameters) are the equilibrium and monolayer gas adsorption capacity (kmol/kg), b is another model constant (1/bar), p_e is adsorption equilibrium pressure (bar).

RESULTS AND DISCUSSION

1. Characterization

1-1. FTIR Analysis

Inorganic material surfacial functional groups can react with the polymer chains and then enhance the gas solubility within the nanocomposites [62,63]. Significant absorption bands of the amine-functionalized ANTs and the prepared membranes were distinguished using FTIR as shown in Figs. 5 and 6. As is observed in Fig. 5, the absorbed water (-OH bands) broad peaks appeared in 3,469 and 1,636 cm^{-1} and were attributed to the Aghion stretch-

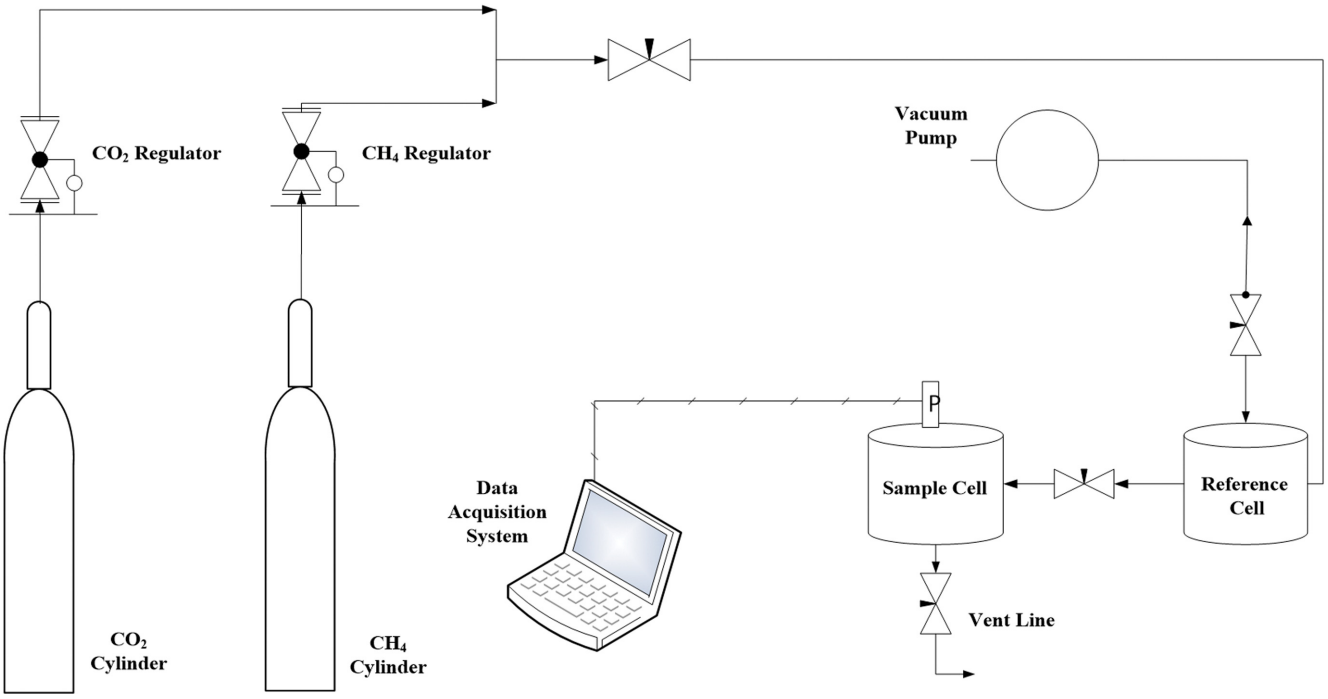


Fig. 4. Schematic representation of the Lab-scale setup for gas adsorption measurement.

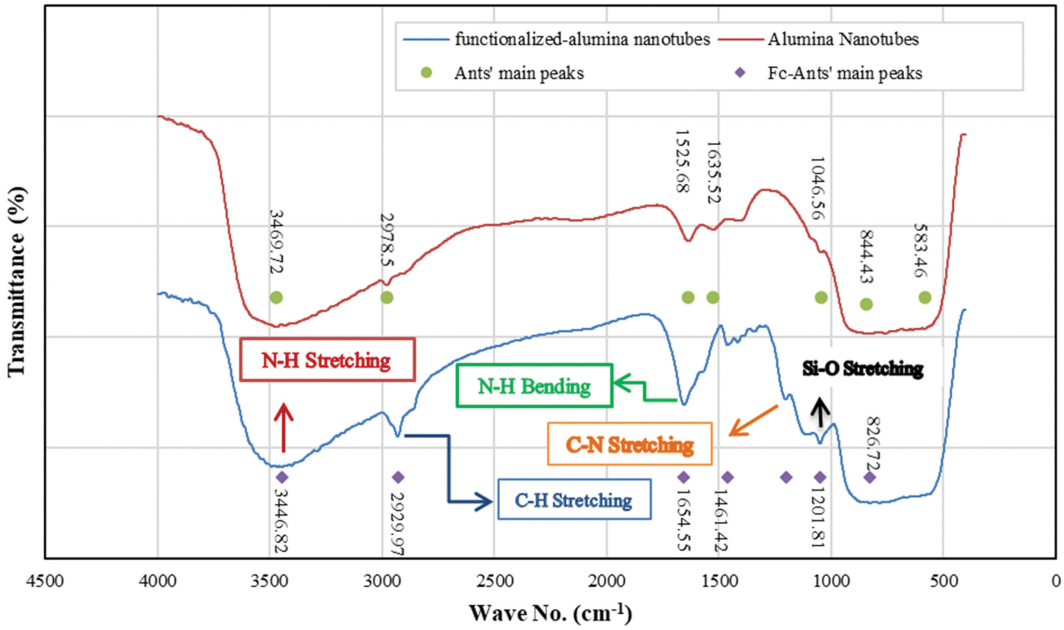


Fig. 5. FTIR spectroscopy of the prepared raw and amine-functionalized ANTs.

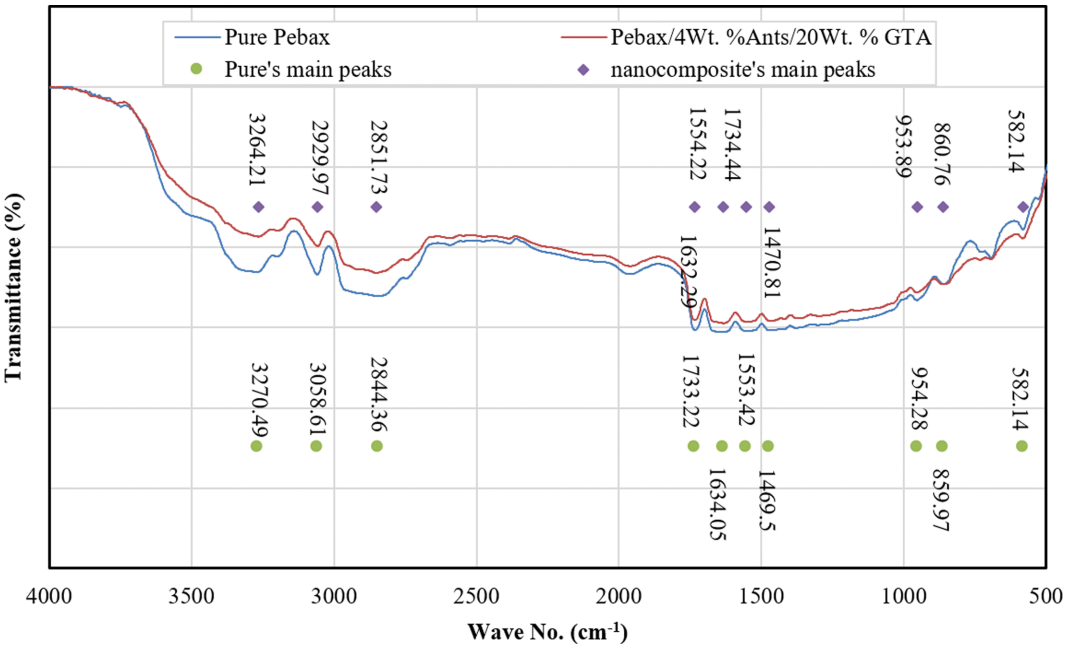


Fig. 6. FTIR spectroscopy of the pristine Pebax and the Pebax/4 wt% ANTs/20 wt% GTA nanocomposite membranes.

ing and bending modes, respectively [42,64]. Two stretching vibrations of the Al-O group appeared in 844 and 583 cm^{-1} [65]. The v_{sym} Al-O-H mode was attributed to the chemically bonded water molecules on the alumina surface, appearing as a weak peak at 1,046.56 cm^{-1} [64].

Fig. 5 also shows adsorption bands of the functional groups after amine functionalization with APTES. The peak at 3,446 cm^{-1} shows that the Al-OH index peaks removed after reaction with silane (APTES) and stretching vibration of the NH_2 group was formed [15]. After reaction with APTES, the stretching bands of Si-O located in 1,049 cm^{-1} also appeared. The band of 2,929 cm^{-1} was attributed to the C-H, -CH_3 and -CH_2 stretching vibrations attributed to the CH_3 and -CH_2 groups of APTES molecule and the band 1,654 cm^{-1} corresponds to the bending vibration of N-H group in silane [40]. The peak at 1,201 cm^{-1} belongs to the stretching vibration of C-N groups. The band of 1,049 cm^{-1} was an indicator of the Al-O-Si linkage stretching vibration [13].

The pristine Pebax membrane and the Pebax/4 wt% ANTs/20 wt% GTA nanocomposite membrane were analyzed using FTIR spectrums which are shown in Fig. 6. Peak at 3,264 cm^{-1} in the

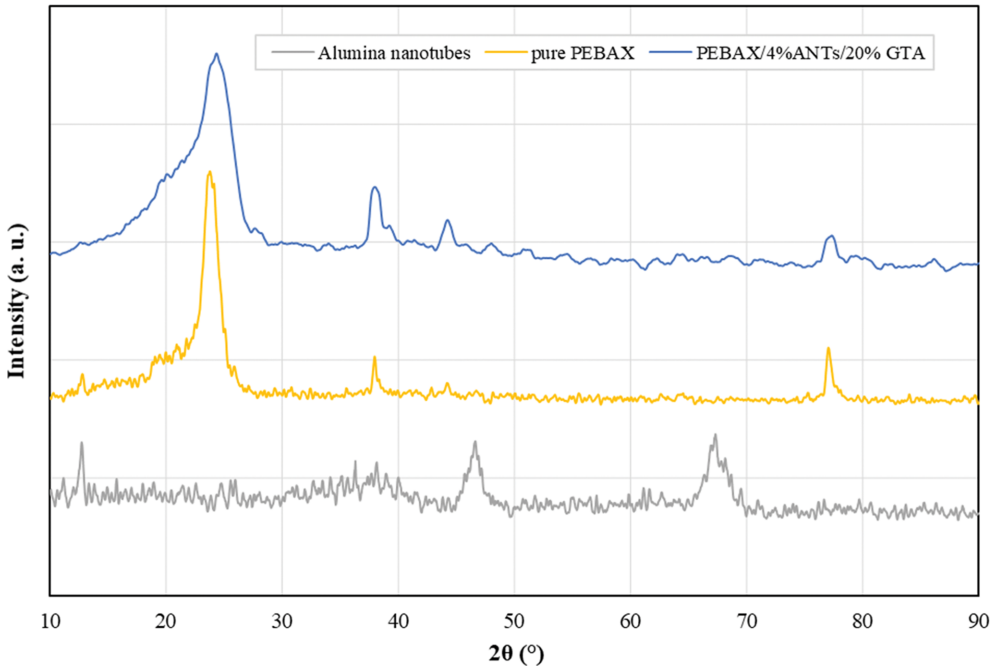


Fig. 7. XRD patterns of the raw ANTs and the pristine Pebax and the Pebax/4 wt% ANTs/20 wt% GTA nanocomposite membranes.

pristine polymeric membrane, represents the stretching vibration of N-H functional groups in the polyamide segment (PA) of Pebax 1657. The 1,632 cm^{-1} band belongs to the stretching frequency of the hydrogen-bonded C=O in H-N-C=O [66]. The peaks at 2,851 and 1,733 cm^{-1} were attributed to the presence of the aliphatic -CH group and saturated esters (O-C=O) [58]. The bending vibration of the N-H group in the PA segment was also characterized at 1,554 cm^{-1}. Moreover, the observed peaks at 2,844 and 1,469 cm^{-1} were related to the bending and stretching vibrations of the C-H aliphatic group, respectively [18].

FTIR spectra of the Pebax/ANTs/GTA nanocomposite membranes reveal that after incorporation of the ANTs, nearly all the signals belonging to the functional groups of the pristine Pebax appeared with a small changes. The changes occurred as the result of interaction between the constituent materials and incorporated ANTs. Interactions including the -OH groups (hydrogen bonding) between the polymer chain and the ANTs were observed in the range of 2,400-3,600 cm^{-1} [42]. A peak at 1,632 cm^{-1} belongs to the saturated esters' C=O stretching vibration, which was shifted to a higher wavenumber of 1,634 cm^{-1} after the ANTs and GTA addition. Carbonyl groups (C=O) in the polyamide segment were also observed at 1,553 cm^{-1}. The main peak at 1,734.44 cm^{-1} corresponding to C=O in H-N-C=O was shifted to 1,732.22 cm^{-1} after GTA addition into the polymer matrix of the nanocomposite membrane [6]. The N-H functional group's peak position was shifted to 3,270 cm^{-1} which proved the interchain hydrogen bonding was partially disturbed after adding ANTs and GTA [11]. These changes show that the added GTA acts as a plasticizer and hinders the hydrogen bonding formation in the hard segment of the polymer chains resulting in the nanocomposite membrane's degree of crystallinity decrement [48]. Hydrogen bonds act as intramolecular bonds in polymeric structures. A low number of intramolecular hydrogen bonds in PA and PE segments lead to closer molecule packing and also higher crystalline solid structures to form. Therefore, the polymer crystallinity degree is determined by the forces inbuilt by intermolecular bonds and also as well as its structural characteristics [67].

1-2. XRD Analysis Results

Fig. 7 represents the XRD patterns of the synthesized ANTs, the pristine, and the nanocomposite membranes. The XRD pattern of the synthesized ANTs proves formation of the gamma phase, and as it can be observed in Fig. 7, all the main peaks of γ-Al_2O_3 including the broad 2θ peaks of 46.49 and 66.93° prove the nanocrystal size of nanotubes and pure cubic γ-Al_2O_3 phase formation [64]. Usually, larger nanoparticles indicate a more intense XRD characteristic peak as a result of the better reflection of the X-ray beam from their crystalline structure larger plane [54]. Two major peaks appeared at 2θs of 12.78 and 23.76° which proved that the copolymer contains crystalline and amorphous PEO and PA segments and building a semi-crystalline structure attributed to the PA groups intermolecular hydrogen bonding [46,68]. It can be noted that for the nanocomposite membranes, the peaks' intensity decreased after addition of GTA and incorporation of ANTs due to the increased content of ANTs and GTA amorphous phases. The interchain hydrogen bonds between the polymer crystalline segments were broken after incorporation of ANTs and even the diffraction peak of 12.78° became almost undetectable. So, the nanocomposite membrane crystallinity lowered, which might enhance its gaseous penetrant permeability through the amorphous regions having lower penetrant mass transport resistance. The ANTs' characteristic peak at 46.49° appeared and proved that the existence of ANTs did not affect the Pebax main peak locations and also the proper distribution of incorporated ANTs within the continuous polymer matrix [6,65]. d-Spacing (intermolecular distance) values

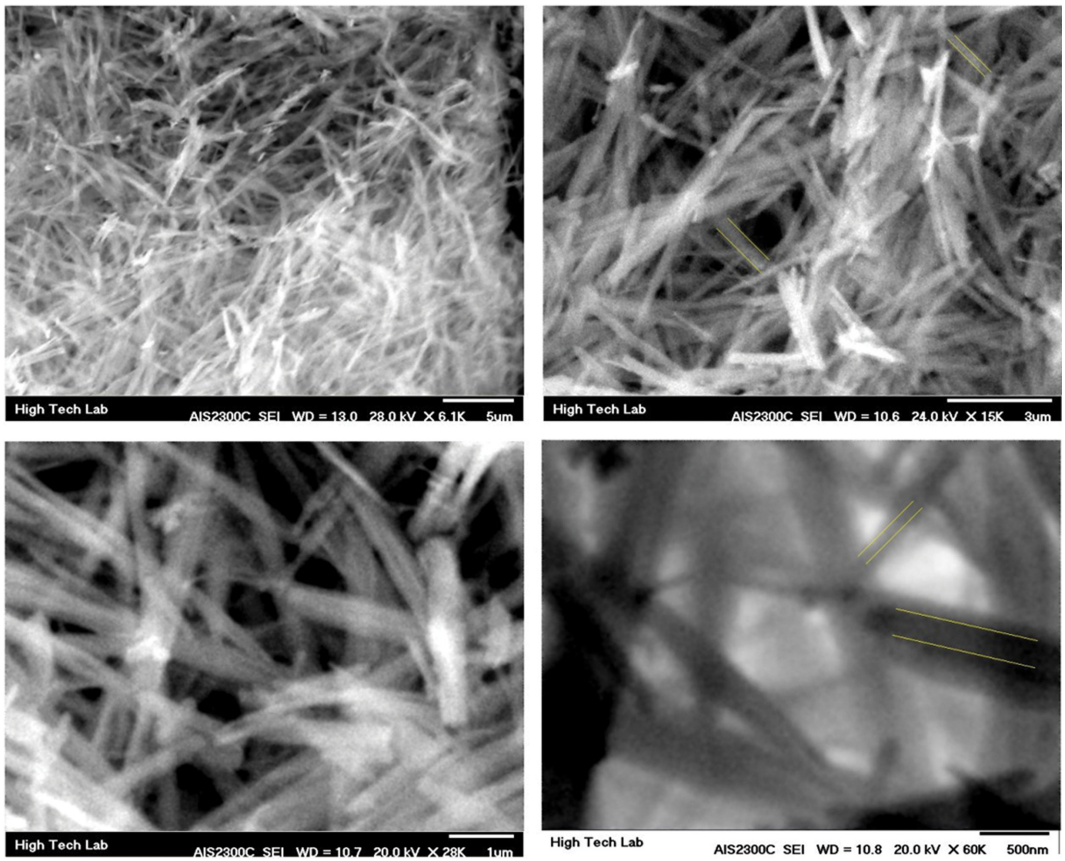


Fig. 8. SEM images of the synthesized ANTs.

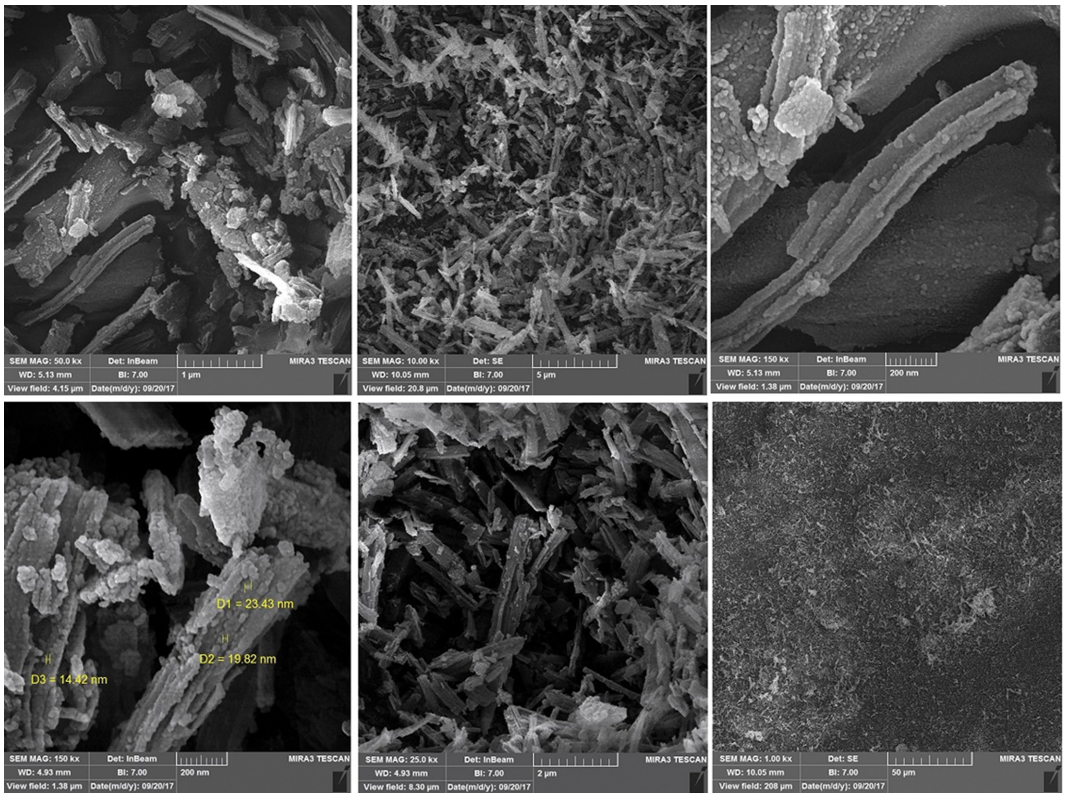


Fig. 9. FESEM images of the synthesized ANTs.

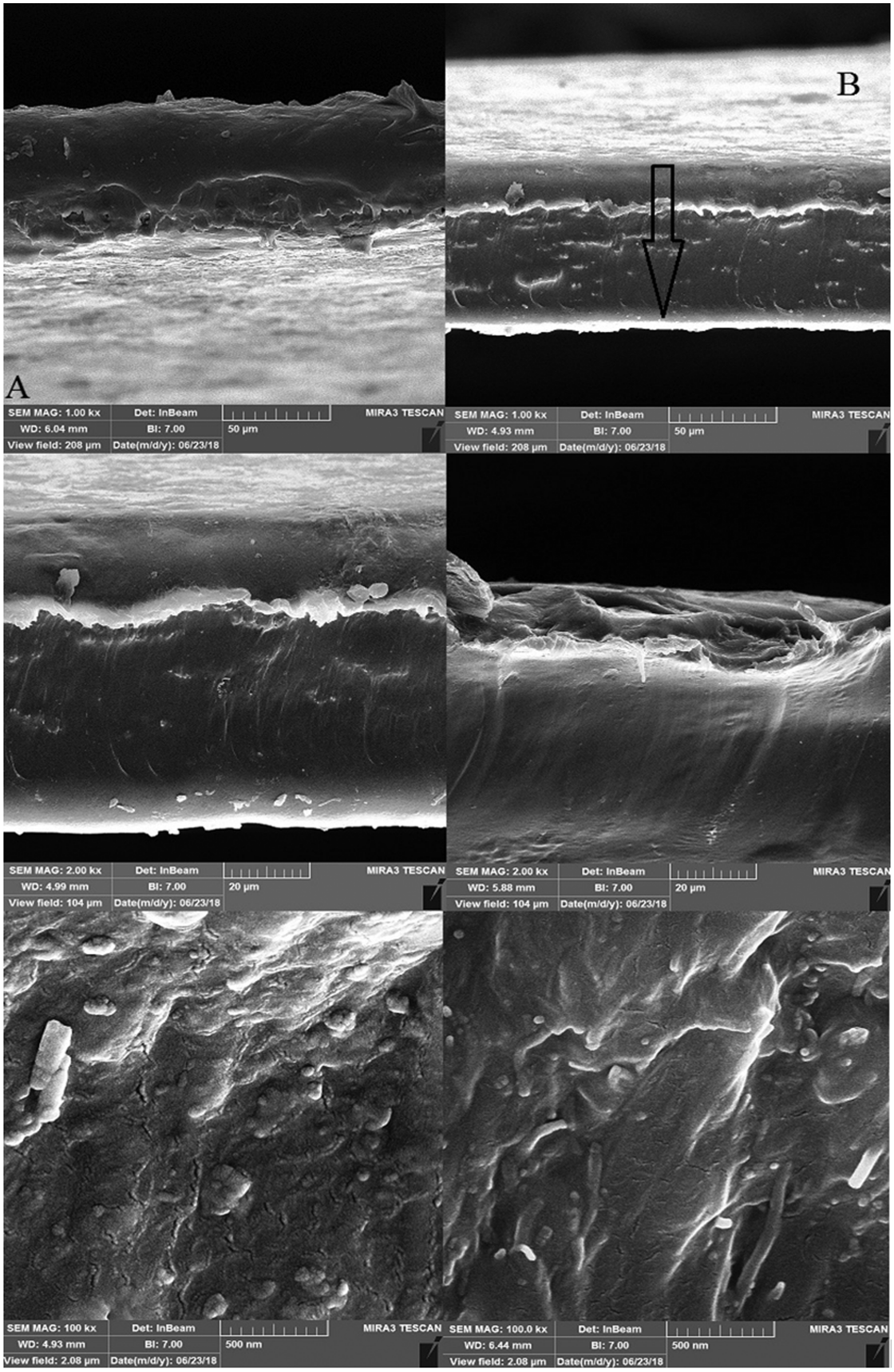


Fig. 10. Different magnification cross-sectional FESEM images of: A) the Pebax/4 wt% ANTs and B) the Pebax/4 wt% ANTs/20 wt% GTA nanocomposite membranes.

of the membranes were calculated using Bragg's law and the main peaks 2θ values to investigate the effects of the modification on the polymer chain wrapping. The results revealed that after the addition of ANTs and GTA, the d-spacing reduced from 3.74 for the pristine polymeric membrane to 3.65 Å for the nanocomposite membranes, which proves the increased interactions between the polymer chains and the incorporated ANTs [69].

1-3. SEM Analysis Results

SEM and FESEM images of the prepared ANTs are presented in Figs. 8 and 9, respectively. According to the images, the inner diameters of the synthesized ANTs are different in size while confidently are in the nanosized range [28]. SEM images have higher resolution as the samples were gold coated; however, for FESEM images, since they were dispersed in the ethanol medium there was agglomeration to some extent and their morphology examination revealed a little nanotube collapse and bundles formed. The ANTs' insignificant shrinking might be attributed to dehydration after calcination [64]. As shown in the SEM images, the diameter of the single tubes was not constant and they are slightly sharper at their both ends than the tube's middle part. All the synthesized tubes have a uniform hollow 1D-nanotubular structure with an estimated average diameter of about 15-45 nm and varying length from to 800 nm to 2 μm [70].

Membrane gas separation performance is profoundly affected by its structure and morphology. Cross-sectional FESEM images of the 4 wt% ANTs incorporated nanocomposite membranes and the Pebax/4 wt% ANTs/20 wt% GTA were provided and are shown in Fig. 10. As is observed, the ANTs filler particle distribution in the polymeric matrix of the nanocomposite membranes is uniform and the membranes have dense structures; meanwhile, a little agglomeration is observed since there were not very robust interactions between the filler particles and macromolecules of continuous polymeric phase. However, there are no formed voids in the interface of filler particles, polymer chains and it can be mentioned that some defect-free nanocomposite membranes were prepared [11]. It was proved that sonication of a mixture containing filler particles decreases the attractive energy of the ANTs and prevents their agglomeration [18]. After GTA addition, the membrane structure uniformity increased compared with the Pebax/4 wt% ANTs, which can be attributed to increased polymer chain mobility after GTA addition resulted in the better dispersion of the ANTs filler particles [6]. Also, the nanocomposite membrane thickness could be estimated from the image as ~85 μm, which is in agreement with those measured by the digital micrometer.

1-4. DSC Analysis Results

The prepared nanocomposite membrane was evaluated by DSC to investigate the ANTs incorporation and the GTA addition on its crystallinity and thermal properties including T_m and T_g. The polymer crystalline regions mainly affect its T_g [42] and the nanocomposite membrane's T_g is affected by its matrix chain rigidity [52]. The interactions of the incorporated ANTs and the added GTA with the matrix polymer chains interrupted the polymer high-ordered packing chains and prevented amide blocks from forming hydrogen bondings. This fact is in good accordance with those of the XRD and the FTIR analysis. The lowered membrane crystallinity is favored by penetrant gaseous transport since their diffusion coefficients were enhanced [67].

The pristine Pebax membrane's T_g was reported as ~−51 °C [46,67] which was correlated with the polyether blocks, and the PEO and the PA6 blocks T_ms was found around 14 and 205 °C, respectively, according to Rabiee et al. [48]. T_m and T_g of GTA were reported as −78 and −68 °C, respectively, by the manufacturer [47]. The Pebax/4 wt% ANTs/20 wt% GTA nanocomposite membrane was analyzed using DSC and the results are shown in Fig. 11. As it is observed, the nanocomposite's T_g value is −58.6 °C, lower than that of the pristine membrane and higher than pure GTA, which corresponds to the PEO segment and shows that GTA and PEO phases are moderate to high miscible [47]. On the other hand, the PA phase's T_g could not be observed by DSC method [6,47]. Detecting melting points of PEO and PA as 12.4 and 205.8 °C

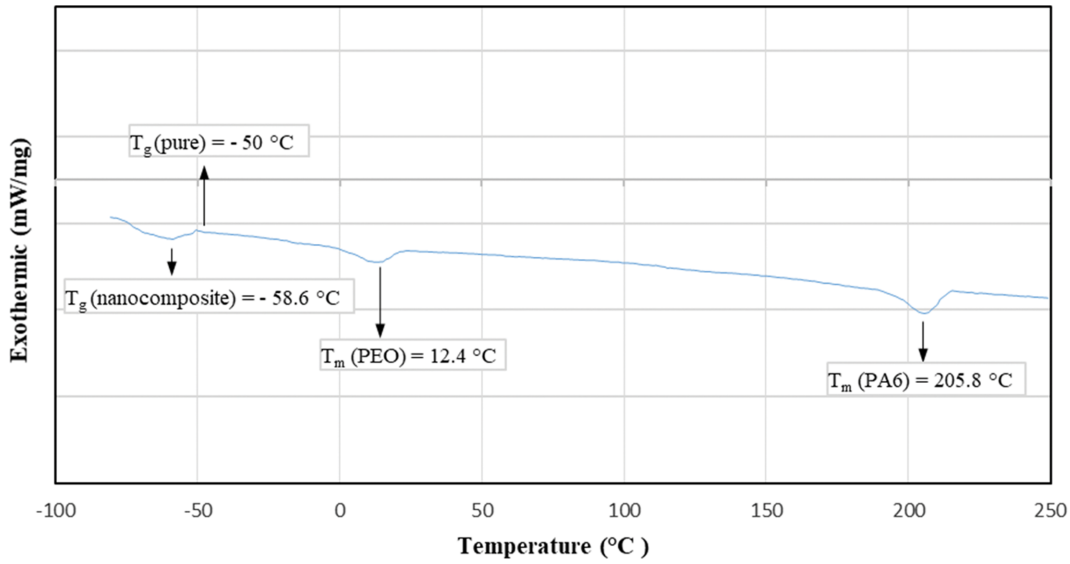


Fig. 11. DSC thermograms of the Pebax/4 wt% ANTs/20 wt% GTA nanocomposite membrane.

shows that GTA, acting as a plasticizer as placed between the polymer chains, increases the nanocomposite matrix chain mobility [71]. ANTs and GTA incorporation in the Pebax matrix resulted in reduction of the matrix crystallinity, i.e., increment in the structure's amorphous parts. The polymer chain rigidity decrement results in providing higher free volumes for the penetrants dissolving and diffusion. Therefore, reduction in the membrane's T_m is favored by both the penetrant solubility and diffusivity. Substituting/reduction the polymer crystalline parts by adding GTA/incorporated ANTs, which have lower adsorption for gases molecules, increases the membrane FFV, and consequently the gaseous penetrant diffusivity. Moreover, this substitution provides more space for the gaseous penetrants and leads to their slightly enhanced solubility in the resultant membrane [6,48]. The Pebax/4 wt% ANTs/20 wt% GTA membrane's T_m can be read from its DSC graph as ~12 and 206 °C and attributed to the PEO and the PA6 crystals melting points, respectively. While slight changes were observed in the melting of the polyether domains, the thermal transition of polyamide block does not seem to be influenced by ANTs incorporation and GTA addition, as the main peak temperature was not changed. The change in polyether segments of the nanocomposite membrane reveals that these parts start to melt at a lower temperature than that of the pristine polymeric membrane [72].

2. The Synthesized ANTs' Adsorption Performance

Adsorption performance of particles is an important indicator affecting their separation performance as a constituent of the nanocomposite membranes. The nanoparticle adsorption capacity depends mainly on their surface area and functional groups like -OH groups and adsorbate gas molecule properties. Also, the adsorbent's gas capture capacity is considerably changed by adsorption operating temperature and pressure, i.e., it is greatly reduced as the adsorption temperature increases [15]. Both ANTs' and grafted ANTs' CO_2 and CH_4 adsorption capacities were measured and are presented in Fig. 12. For both particles, the CO_2 adsorption capacity was higher than those for CH_4 molecules. Also, their CO_2 and CH_4 uptake increased as the adsorption pressure increased, which could be attributed to the strong quadropolarity interactions of CO_2 molecules and ANTs' functional groups, and/or their unsaturated open tubes while nonpolar gases like CH_4 have fewer affinity/interactions toward the adsorbent functional groups [73]. Subsequently, the adsorbed amount of CH_4 molecules on the nanoparticles was lower, which could be attributed to the symmetric vibrations. It can be also mentioned that, momentary polarity of molecules enhances their affinity toward the adsorbent functional groups [15]. Measured gas adsorption data indicated that ANTs have greater potential to adsorb CO_2 molecules than the grafted ANTs. Although the aliphatic amine peak was detected in FTIR spectrum at 2,929.97 cm^{-1} for the grafted ANTs; however, it seems that the interactions between these groups and the gases molecules were not strong enough, and also APTES functional group site density on the surface grafted ANTs prevents further gases adsorption via restricting the gas molecule penetration path [43]. APTES have three ethoxy groups and provide numerous coupling agents that reduce surface area, leading to lowering CO_2 molecule adsorption reduction [74].

3. Membrane Gas Permeability

3-1. Effect of the Nanocomposite Membrane's ANTs Loadings

The importance of choosing the continuous and the dispersed phases in fabricating nanocomposite membranes is vital as both phases should be compatible with each other and also have desired performance. Otherwise, poor adhesion between these two phases leads to some defects on their interfaces and decreases the resultant nanocomposite membrane's separation performance [10].

Polar molecules in ethylene oxide (EO) groups and oxygen bonds in the Pebax soft segments together with their quadratic characteristics make the polymer have a significant affinity toward acidic gases like CO_2 [67]. According to the solution-diffusion model, the pristine membrane gaseous penetrant solubility and diffusivity have a determining role in the CO_2 separation/removal from small gas molecules like CH_4 and N_2 [75]. As mentioned above, due to higher CO_2 critical temperature (i.e., higher condensability) and smaller kinetic diameter (0.33 nm compared with that of CH_4 as 0.38 nm), CO_2 is expected to have higher permeability through the Pebax membrane [76]. The diffusion rate in semicrystalline poly-

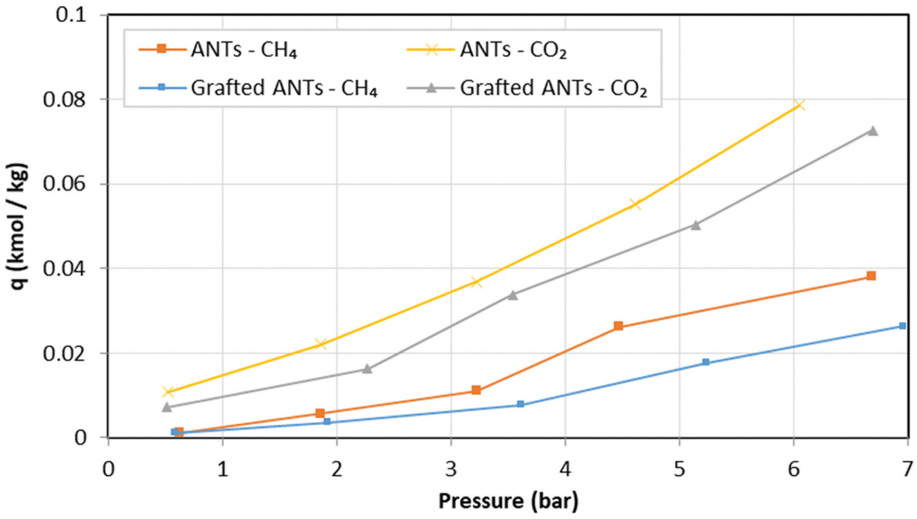


Fig. 12. Measured adsorption capacity of the as prepared and the grafted ANTs.

mers like Pebax relies upon both polymer properties, such as free volume and preparation parameters, along with factors during membrane preparation and permeability measurement. In almost all researches, EtOH/Water was applied as the solvent to prepare Pebax solution due to its accessibility and low cost [77,78]. The casting solution's solvent type strongly affects the resultant membrane morphology and structure during both solution preparation and film-forming step since the used solvent acts as a temporary spacer and reduces the polymer chain packing density [79]. Nevertheless, in some investigations, DMF was selected as the Pebax solvent. DMF has closer solubility parameters to the Pebax than those of EtOH/Water mixture, which leads to the better dissolving of the polymer granules [11,60]. The high discrepancy between the polymer and EtOH/Water solubility parameters led to the formation of denser membrane structure and lowering penetrants permeabilities [80]. Furthermore, the DMF molar volume (as 77.1 cm^3/mole) is higher than that of EtOH/Water (as 36.14 cm^3/mole), which leads to an increment of the resultant membrane FFV and finally its gas permeability enhancement [81]. So, it is anticipated that the prepared membranes using DMF, as the solvent, have higher permeability than those prepared by EtOH/water mixture. The higher boiling point of DMF (as 153.2 °C) than that of EtOH/water mixture (75 °C) is another factor leading to a lower evaporation rate during the membrane drying process and more interconnections in the membrane matrix. As a consequence, the dissolved polymer chains had more time to form higher-ordered structures, which resulted in the membrane crystallinity increment and FFV decrement. On the other hand, the main structural part of the prepared membranes using EtOH/Water mixture is amorphous [82]. Isanejad et al. investigated effects of different solvents on the morphology and permeation reate of poly(ether-block-amide). They proposed that membranes fabricated using DMF solvent have higher crystallinity content and permeability than those of fabricated using the mixture of EtOH/Water [80]. Another important reason for DMF application as the solvent is its higher viscosity which causes the casting solution to have higher stability after its cooling from the oil bath to ambient temperature. This stability hinders the ANTs precipitation and their agglomeration during the membrane drying process [15]. Taking into account all the above-mentioned parameters, including molar volume, boiling point, solubility parameters and higher viscosity of the solvent, the prepared pristine and nanocomposite membranes using DMF as the solvent have higher penetrant permeability and selectivity than those prepared by EtOH/water as the solvent. The ideal CO_2/CH_4 selectivity for the pure membrane prepared by DMF solvent was also higher than those prepared using EtOH/water solvent, which reveals the diffusion rate of CH_4 molecules was not significantly affected. The CO_2 permeability through different prepared membranes was much higher than that of CH_4, which could also be attributed to the rubbery PEO blocks in Pebax. PEO blocks have strong interactions with the polar gases (i.e., CO_2) over the non-polar gases (i.e., CH_4) [11].

The pure gas permeability through the pristine and the nanocomposite membranes prepared using the EtOH/water mixture and DMF solvents at 5 bar and 35 °C is presented in Tables 1 and 2, respectively. Incorporation of inorganic materials in the polymeric matrices usually increases both the penetrant diffusivity and solubility due to their molecular sieving effect. As it can be observed, as the ANTs loading in the Pebax matrix increased up to 10 wt%, both permeability of CO_2 and CH_4 through all prepared membranes increased. As the ANT filler particles were incorporated in the polymeric membrane matrix, their gas permeability enhanced due to the polymer chain packing disruption, and consequently the polymer's FFV and chains' mobility increments. Gaseous molecule penetrants permeate faster through lower mass transfer resistance parts of nanotubes than the polymer matrix [19]. It also can be ascribed to the better interaction between the CO_2 molecules with -OH functional groups on the surface of the ANTs, or with polar groups of Pebax, as detected by FTIR analysis [78]. The membrane CO_2 permeability was enhanced by incorporation of nanotubes in the range of 0-10 wt% from 117.83 to 161.97 Barrer using DMF solvent and from 101.89 to 129.61 Barrer using EtOH/water as the solvent. These trends reveal that pure gas permeability values increased as higher ANTs were incorporated into the polymer matrix, while the solvent type also has a significant impact on the prepared nanocomposite membrane separation performance. On the other hand, the presence of the ANTs probably creates some voids because of their different inorganic nature from the organic polymer matrix at their interfaces. Void formation around the filler particles has a diverse impact on the membrane separation performance, since they could improve the gas penetrant permeability while deteriorating their separation factor [83].

Reduction in membrane crystallinity and enhancement in sorption capacity is due to a probably different phase of the nanotubes and the polymeric matrix interface, which all result in the pene-

Table 1. Pure gas permeability of the Pebax/ANTs nanocomposite membrane using a mixture of EtOH/water (70/30) solvent at 35 °C and 5 bar

ANTs loading (wt%)	Permeability±SD (Barrer)		Ideal selectivity
	CO_2	CH_4	
0	101.89±2.8	6.66±0.33	15.30
2	106.26±3.6	6.58±0.4	16.15
4	111.44±2.6	6.72±0.36	16.58
6	118.25±4.4	6.92±0.34	17.09
8	123.97±4.1	7.01±0.39	17.68
10	129.61±3.3	7.27±0.31	17.82

Table 2. Pure gas permeability of the Pebax/ANTs nanocomposite membranes using DMF solvent at 35 °C and 5 bar

ANTs loading (wt%)	Permeability±SD (Barrer)		Ideal CO_2/CH_4 selectivity
	CO_2	CH_4	
0	117.83±1.7	6.47±0.78	18.21
2	138.36±5.4	7.64±0.54	18.11
4	148.24±2.2	8.2±0.29	18.08
6	154.46±3.4	8.76±0.38	17.63
8	159.31±4.2	9.32±0.51	17.09
10	161.97±3.6	9.59±0.46	16.89

trant transport acceleration through the nanocomposite membranes [60]. The ideal selectivity of the prepared membranes using DMF solvent decreased from 18.21 to 16.89 with increasing ANTs' loading from 0 to 10 wt%. The CH_4 permeability increment was a little higher than that of CO_2 compared with the prepared membranes using EtOH/water mixture as the solvent. Lower selectivity may likely be ascribed to the unfavorable dispersion of nanotubes at higher loading or higher tortuous diffusion path; those reduce the gaseous penetration rate through the membrane free volume [9,62]. However, ideal selectivity of the prepared membranes using EtOH/Water solvent increased from 15.30 to 17.82 as the ANTs' loading increased to 10 wt%, which could be attributed to the improvement of the gaseous penetrant diffusivity and solubility in the prepared nanocomposite membranes. As the nanoparticles were incorporated in the polymer matrix, the penetrant gas pair solubility selectivity enhanced more than their diffusivity selectivity, which could be attributed to formed spaces in the interface of polymer - agglomerated nanotubes. These spaces led to the greater adsorption capacity of small gases compared with the other ones and consequently higher gas selectivity in nanocomposite membrane [84].

For the grafted-ANTs (Tables 3 and 4) at lower filler particles loadings (i.e., 2 wt%), the nanocomposite membrane permeability decreased due to the membranes FFV and chain mobility reduction. At the higher ANTs loadings, the membrane CO_2 permeability enhanced due to increasing the functional group density on the filler particles and their more and more interaction with the CO_2 molecules resulting in the membrane CO_2 solubility increment [66]. At the lower nanocomposite membrane ANTs loading, the gaseous penetrant permeability decreased while their selectivity increased due to the matrix polymer chain rigidification, i.e., lowering their mobility, resulting in higher selective nanoparticle interfaces [69]. When there was good interfacial adhesion of the polymeric chains to the surface of filler particles, the polymer matrix's FFV decreased in the filler particles neighboring due to the lowered mobility of the polymer chains. In contrast, weak adhesion of the filler particle - polymer chains leads to formation of some interfacial nanovoids and these increase the penetrant permeability through the nanocomposite membrane, i.e., facilitating their penetrant transport through and maybe reducing their selectivity [85].

Table 3. Pure gas permeability of the Pebax/grafted-ANTs nanocomposite membranes using DMF solvent at 35 °C and 5 bar

Grafted-ANTs loading (wt%)	Permeability±SD (Barrer)		Ideal CO_2/CH_4 selectivity
	CO_2	CH_4	
0	117.83±1.7	6.47±0.78	18.21
2	103.75±2.4	5.39±0.66	19.25
4	116.65±1.8	6.32±0.43	18.46
6	120.52±3.6	6.65±0.78	18.12
8	125.47±4.5	7.04±0.52	17.82
10	131.79±5.1	7.54±0.38	17.48

Table 4. Pure gas permeability of the Pebax/grafted-ANTs nanocomposite membranes using a mixture of EtOH/Water (70/30) solvent at 35 °C and 5 bar

Grafted-ANTs loading (wt%)	Permeability±SD (Barrer)		Ideal CO_2/CH_4 selectivity
	CO_2	CH_4	
0	101.89±2.8	6.66±0.33	15.30
2	89.86±2.5	5.12±0.32	17.55
4	95.4±3.1	5.58±0.57	17.10
6	99.75±2.3	5.92±0.43	16.85
8	112.17±4.8	6.86±0.47	16.35
10	119.34±3.2	7.34±0.52	16.26

As the grafted ANTs loading increased, the resultant nanocomposite membranes revealed higher CO_2 and CH_4 permeability due to the polymer matrix chain packing disruption by their incorporation [85]. Therefore, at the nanoparticle lower loadings, the polymer chain rigidification is the predominant phenomenon in the nanocomposite membrane structure, while at their higher loadings the chain packing disruption increases the membrane FFV. After the ANTs' modification, CO_2 molecule transport through grafted-ANTs loaded nanocomposite membranes is facilitated. However, the CH_4 molecule transport through nanocomposite membranes prepared by grafted ANTs was not considerably affected by their interaction with the functional groups and their higher permeation rate obtained only through the increased FFV of the nanocomposite membrane. Although using silane coupling agents potentially could reduce the interfacial defects around the filler particles, partial filler particle agglomeration observed at the higher filler particles loadings increases and decreases the resultant membrane permeability and selectivity, respectively [43]. Moreover, at higher loading of the filler particles incorporation within the polymer matrix, particles tend to agglomerate and/or sediment, which might result in non-selective undesired void formation around them. The formed voids have adverse effects on the performance of the nanocomposite membrane separation since they starve the incorporated filler particles (i.e., ANTs) and frustrate the aim of their incorporation. The probable formed void size may be larger than both molecular volumes of the CO_2 and the CH_4, i.e., sieve-in-a-cage case of the nanocomposite membrane structure resulting in both gaseous molecules faster diffusion through the membranes [41]. Therefore, at higher grafted ANTs loading, CH_4 molecules with a kinetic diameter larger than the CO_2 molecules transport slightly faster, and consequently, CO_2/CH_4 selectivity of the prepared membranes using DMF declines [40]. APTES is an aminosilane that has three alkoxys (methoxy, CH_3O) forming a vast number of coupling sites on the external surface of their attached ANTs particles. These sites are formed through a silylation reaction, which results in carbamate ion formation. These ions lower the gaseous' molecules access to the filler particles [41,86].

Selectivity of the membranes prepared using a solvent of EtOH/Water mixture, at higher ANTs loadings is greater than that of the pristine membrane; however, the growth rate of membrane selectivity decreased as the grafted-ANTs were incorporated. The grafted-ANTs incorporated membranes' CO_2 and CH_4 permeability prepared using DMF solvent are increased (Table 4). Subsequently, at higher grafted-ANTs loading, the nanocomposite membrane permeability increment rate for CH_4 is higher. The 10 wt% grafted-

Table 5. Pure gases permeability of the Pebax/4 wt% ANTs/GTA nanocomposite membranes at 35 °C and 5 bar

GTA (wt%)	Permeability±SD (Barrer)		Ideal CO_2/CH_4 selectivity
	CO_2	CH_4	
0	148.24±2.2	8.2±0.29	18.08
10	156.05±2.1	8.72±0.33	17.90
20	169.8±2.9	9.55±0.52	17.78
30	183.23±5.3	10.51±0.61	17.43
40	204.73±3.8	11.83±0.45	17.31

ANTs incorporated nanocomposite membrane reveals better separation performance than that of the pristine membrane as 119.34 Barrer for CO_2 permeability and 16.26 for CO_2/CH_4 selectivity.

3-2. Effect of GTA Addition

As reported in Table 5, the CO_2 and CH_4 permeability was enhanced as GTA content in the nanocomposite membrane increased. Based on the FTIR result, by the addition of low molecular weight GTA into the polymer matrix, interactions of the Pebax polymer chains were interrupted and the membrane matrix chain mobility increased to form some interconnection pathways between polymer chains. By the matrix GTA content increment, the penetrant permeability, especially for CO_2 molecules, increased, which proves GTA enhances polymer permeation rates through the membranes via gaseous penetrant diffusivity increment in the softened segments of the membrane matrix [47]. Hence, permeation rate of the gaseous penetrants increased due to growth in diffusivity depending on their relative molecular sizes. Moreover, GTA acts as a matrix plasticizer and can provide more space between the polymer chains (i.e., higher FFV), which provides higher mobility toward the larger molecules via enhancement of their diffusivity in the matrix [87]. Consequently, the nanocomposite's FFV and subsequently the diffusion coefficient of the penetrants through it increase. This increment for the larger CH_4 molecules in kinetic diameter was even though higher than that of CO_2 which resulted in keeping the CO_2/CH_4 ideal selectivity nearly constant or slightly decreased. Therefore, the higher GTA content in the membrane results in the higher CH_4 molecule diffusivity. The CO_2-phillic and high-oxygenated GTA material could also enhance CO_2 solubility through the membrane matrix. Oxygen atoms in the GTA's acetate group can interact with polar gases like CO_2 molecules, which is responsible for increasing their solubility coefficient [47,88]. Rabiee et al. proved that by GTA addition both gaseous penetrant diffusion and solubility coefficients increased; however, increment of the penetrant diffusion coefficients is greater than their solubility coefficients in Pebax1657/GTA blended membranes. D_{CO_2}/D_{CH_4} ratio in the blended membranes was reduced as their GTA content was increased. However, their solubility selectivity S_{CO_2}/S_{CH_4} ratio did not considerably change, resulting in a slight reduction of the membrane permselectivity [48]. According to the prepared nanocomposite membrane XRD results, their crystallinity was lower than that of the pristine one, which is favorable for penetrant solubility enhancement since the matrix's nonadsorbing crystal segments are not permeable. Also, DSC analysis results illustrated that the nanocomposite membrane's T_g decreased after the addition of GTA to the polymer matrix [58,89]. Moreover, according to the FTIR analysis, some GTA molecules might be captured into or onto the ANTs, or form hydrogen bonds that interrupts the intermolecular interactions in the nanocomposite membrane structure

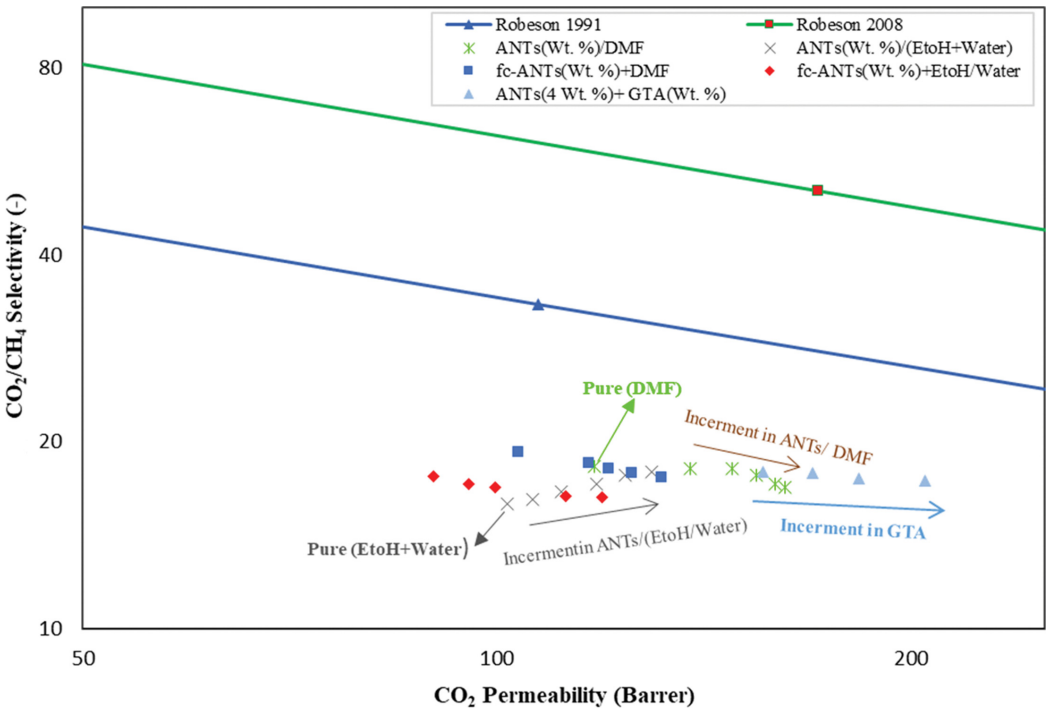


Fig. 13. CO_2/CH_4 selectivity and CO_2 permeabilities of Pebax1657-based nanocomposite membranes at 35 °C and 5 bar in the Robeson upper bound limit chart.

[6]. Reduction in ideal CO_2/CH_4 selectivity proves that penetrant permeation was dominated by diffusion more than solubility since growth in CH_4 diffusion was moderately higher than that of CO_2 [90]. Note that the defect-free polymer/filler interface, with no agglomeration, was the result of the ANTs homogeneous dispersion in the casting solution using ultrasonic waves.

3-3. Separation Performance of the Prepared Nanocomposite Membranes in the Robeson Chart

Passing over the Robeson upper bound limit, which was proposed first in 1991 and then revised in 2008, is the cardinal purpose of almost all studies regarding membrane gas separation. To evaluate effects of different carried out modifications, including the incorporation of the as-prepared ANTs and the grafted-ANTs along with GTA blending on the gas separation performance of the current study's prepared membranes, the obtained data, at 35 °C and 5 bar, are plotted in the Robeson upper bound limit chart as is shown in Fig. 13. As can be noticed, CO_2/light gas selectivity was not improved and there is no passing over the Robeson upper bound limit; meanwhile, there is considerable increment in their CO_2 permeability compared with that of the neat membrane. For instance, the Pebax/4 wt% ANTs/40 wt% GTA exhibited the CO_2 permeability of 204.73 Barrer, and the ideal CO_2/CH_4 selectivity of 17.306 (73.75% increment in CO_2 permeability and 4.96% reduction in CO_2/CH_4 selectivity compared with the pristine Pebax 1657 membrane), becomes closer to the 1991 Robeson upper bound limit [2,91].

CONCLUSION

Alumina nanotubes (ANTs) were synthesized via a hydrothermal method and incorporated in the range of 0-10 wt% within Pebax-based membranes using different solvents of EtOH/Water mixture and DMF. The gaseous penetrant permeability increased in all prepared membranes. However, their selectivity decreased as the DMF solvent was employed for the membrane preparation, which could be attributed to the weak compatibility of the solvent and the ANTs. The prepared nanocomposite membranes' CO_2/CH_4 selectivity trend was reversed by using the mixture of EtOH/Water as the solvent. FESEM results of Pebax/4 wt% ANTs and Pebax/4 wt% ANTs/20 wt% GTA revealed that the membranes were defect-free. The DSC results showed that after the ANTs incorporation and addition of GTA, T_g of the resultant nanocomposite membrane decreased (i.e., lower crystallinity), and the XRD patterns also proved that the diffraction peak intensity and the crystallinity structure of the nanocomposite membranes were decreased. The prepared ANTs were further modified with an aminosilane as the grafting agent, and FTIR results confirmed the success of functionalization. Incorporation of grafted-ANTs increased the resultant membranes CO_2/CH_4 selectivity but decreased both gaseous penetrant permeability at their lower loading, while at higher loading the trends were reversed. The weak interface adherence of the polymer-fillers and the filler particles agglomeration caused the formation of non-selective voids around them. Eventually, GTA was added to the nanocomposite membrane matrix in the range of 0-40 wt%. The nanocomposite membrane matrix CO_2 solubility was originally high and further increased by addition of GTA content in the matrix due to more plasticization effect of CO_2. The Pebax/4 wt%ANTs/40 wt% GTA resulted in 73.75% enhancement in permeability compared with the pristine membrane, while its CO_2/CH_4 ideal selectivity reduced by 4.96%. These facts show the potential for further investigation of these nanocomposite membranes and further promoting them for gas sweetening applications.

ACKNOWLEDGEMENT

The paper's authors warmly acknowledge the Iran Nanotechnology Innovation Council (INIC) for its financial support.

NOMENCLATURE

n	: an integer number [-]
D	: diffusion coefficients [cm^2/s]
d	: *d*-spacing [Å]
p_e	: equilibrium adsorption gas pressure [bar]
q_e	: equilibrium gas adsorption capacity [kmol/kg]
V_g	: gas velocity [m/s]
P	: gas permeability [Barrer]
T_g	: glass transition temperature [°C]
b	: Langmuir adsorption isotherms model parameter [1/bar]
T_m	: melting point [°C]
A	: membrane effective area [cm^2]
FFV	: membrane fraction free volume [-]
α_{CO_2/CH_4}	: membrane ideal CO_2/CH_4 selectivity [-]
V	: membrane permeate side volume [cm^3]
q_m	: monolayer gas adsorption capacity [kmol/kg]
T	: operating temperature [K]
t	: permeation time [s]
θ	: scattering angle [°]
SD	: standard deviation [Barrer]
p_s	: standard pressure [cm Hg]
T_s	: standard temperature [K]
Δp	: transmembrane pressure [mm Hg]
λ	: wavelength [Å]

REFERENCES

1. Y. Xiao, B. T. Low, S. S. Hosseini, T. S. Chung and D. R. Paul, *Prog. Polym. Sci.*, **34**(6), 561 (2009).
2. X. Guo, H. Huang, Y. Ban, Q. Yang, Y. Xiao, Y. Li, W. Yang and C. Zhong, *J. Membr. Sci.*, **478**, 130 (2015).
3. B. Yu, H. Cong, Z. Li, J. Tang and X. S. Zhao, *J. Appl. Polym. Sci.*, **130**(4), 2867 (2013).
4. L. M. Robeson, *J. Membr. Sci.*, **320**(1), 390 (2008).
5. F. Dorosti, M. Omidkhah and R. Abedini, *J. Nat. Gas. Sci. Eng.*, **25**, 88 (2015).
6. D. Zhao, J. Ren, Y. Wang, Y. Qiu, H. Li, K. Hua, X. Li, J. Ji and M. Deng, *J. Membr. Sci.*, **521**, 104 (2017).
7. X. Ren, J. Ren and M. Deng, *Sep. Purif. Technol.*, **89**, 1 (2012).
8. E. Ahmadpour, A. A. Shamsabadi, R. M. Behbahani, M. Aghajani and A. Kargari, *J. Nat. Gas. Sci. Eng.*, **21**, 518 (2014).
9. V. Martin-Gil, A. López, P. Hrabanek, R. Mallada, I. Vankelecom and V. Fila, *J. Membr. Sci.*, **523**, 24 (2017).

10. A. Jomekian, R. M. Behbahani, T. Mohammadi and A. Kargari, *J. Nat. Gas. Sci. Eng*., **31**, 562 (2016).
11. N. Azizi, T. Mohammadi and R. M. Behbahani, *Chem. Eng. Res. Des*., **117**, 177 (2017).
12. M. H. Nematollahi, S. Babaei and R. Abedini, *Korean J. Chem. Eng*., **36**(5), 763 (2019).
13. T. Lakshmikandhan, A. Chandramohan, K. Sethuraman and M. Alagar, *Des. Monomers Polym*., **19**(1), 67 (2016).
14. S. G. Lovineh, M. Asghari and G. Khanbabaei, *Appl. Surf. Sci.*, **318**, 176 (2014).
15. M. Isanejad and T. Mohammadi, *Mater. Chem. Phys*., **205**, 303 (2018).
16. L. V. Vinogradova, G. A. Polotskaya, A. A. Shevtsova and A. Y. Alent'ev, *Polym. Sci. Series A*, **51** (2), 209 (2009).
17. D. Q. Vu, W. J. Koros and S. J. Miller, *J. Membr. Sci*., **211**(2), 311 (2003).
18. N. Azizi, M. Arzani, H. R. Mahdavi and T. Mohammadi, *Korean J. Chem. Eng*., **34**(9), 2459 (2017).
19. S. S. Swain, L. Unnikrishnan, S. Mohanty and S. K. Nayak, *Korean J. Chem. Eng*., **34**(8), 2119 (2017).
20. B. Ghalei, A. Pournaghshband Isfahani, M. Sadeghi, E. Vakili and A. Jalili, *Polym. Adv. Technol.*, **29**(2), 874 (2018).
21. L. Li, T. Wang, Q. Liu, Y. Cao and J. Qiu, *Carbon*, **50**(14), 5186 (2012).
22. R. Mahajan, R. Burns, M. Schaeffer and W. J. Koros, *J. Appl. Polym. Sci*., **86**(4), 881 (2002).
23. G. Castruita-de León, C. Y. Yeverino-Miranda, A. d. J. Montes-Luna, H. I. Meléndez-Ortiz, G. Alvarado-Tenorio and L. A. García-Cerda, *J. Appl. Polym. Sci.*, **137**, 48286 (2019).
24. Q. Zhang, S. Luo, J. R. Weidman and R. Guo, *Polymer*, **131**, 209 (2017).
25. M. Arjmandi, M. Pakizeh and O. Pirouzram, *Korean J. Chem. Eng*., **32**(6), 1178 (2015).
26. E. V. Perez, K. J. Balkus, J. P. Ferraris and I. H. Musselman, *J. Membr. Sci.*, **328**(1), 165 (2009).
27. F. Huang, A. T. Rad, W. Zheng, M.-P. Nieh and C. J. Cornelius, *Polymer*, **108**, 105 (2017).
28. C. Bae, H. Yoo, S. Kim, K. Lee, J. Kim, M. M. Sung and H. Shin, *Chem. Mater*., **20**(3), 756 (2008).
29. A. B. Martinson, J. W. Elam, J. T. Hupp and M. J. Pellin, *Nano Lett*., **7**(8), 2183 (2007).
30. J. Hu, T. W. Odom and C. M. Lieber, *Acc. Chem. Res*., **32**(5), 435 (1999).
31. Y. Zhang, Y. Xu, Y. Lu, L. Zhao and L. Song, *Nanotech*., **24**(31), 315701 (2013).
32. S. P. Albu, A. Ghicov, J. M. Macak, R. Hahn and P. Schmuki, *Nano Lett*., **7**(5), 1286 (2007).
33. J. M. Macak, H. Tsuchiya, A. Ghicov and P. Schmuki, *Electrochem. Commun*., **7**(11), 1133 (2005).
34. S. Berger, A. Ghicov, Y.-C. Nah and P. Schmuki, *Langmuir*, **25**(9), 4841 (2009).
35. M.-H. Seo, M. Yuasa, T. Kida, J.-S. Huh, N. Yamazoe and K. Shimanoe, *Procedia Chemistry*, **1**(1), 192 (2009).
36. F. Song, Y. Zhao and Q. Zhong, *Int. J. Electrochem. Sci*., **7**, 2513 (2013).
37. M. Trueba and S. P. Trasatti, *Eur. J. Inorg. Chem*., **2005**(17), 3393 (2005).
38. J. Baltrusaitis, J. Schuttlefield, E. Zeitler and V. H. Grassian, *Chem. Eng. J*., **170**(2-3), 471 (2011).
39. C. Chen and W.-S. Ahn, *Chem. Eng. J*., **166**(2), 646 (2011).
40. M. Junaidi, C. Khoo, C. Leo and A. Ahmad, *Micropor. Mesopor. Mater*., **192**, 52 (2014).
41. A. E. Amooghin, M. Omidkhah and A. Kargari, *J. Membr. Sci*., **490**, 364 (2015).
42. E. Ameri, M. Sadeghi, N. Zarei and A. Pournaghshband, *J. Membr. Sci*., **479**, 11 (2015).
43. T. W. Pechar, S. Kim, B. Vaughan, E. Marand, M. Tsapatsis, H. K. Jeong and C. J. Cornelius, *J. Membr. Sci*., **277**(1-2), 195 (2006).
44. M. Laghaei, M. Sadeghi, B. Ghalei and M. Shahrooz, *J. Membr. Sci*., **513**, 20 (2016).
45. A. Jomekian, B. Bazooyar, R. M. Behbahani, T. Mohammadi and A. Kargari, *J. Membr. Sci*., **524**, 652 (2017).
46. S. Wang, Y. Liu, S. Huang, H. Wu, Y. Li, Z. Tian and Z. Jiang, *J. Membr. Sci*., **460**, 62 (2014).
47. S. Feng, J. Ren, Z. Li, H. Li, K. Hua, X. Li and M. Deng, *Int. J. Greenh. Gas. Con*., **19**, 41 (2013).
48. H. Rabiee, M. Soltanieh, S. A. Mousavi and A. Ghadimi, *J. Membr. Sci*., **469**, 43 (2014).
49. M. Auta and B. H. Hameed, *Chem. Eng. J*., **253**, 350 (2014).
50. J. Esmaili and M. R. Ehsani, *JEAS*, **3**(02), 57 (2013).
51. A. Tena, L. Fernández, M. Sánchez, L. Palacio, A. Lozano, A. Hernández and P. Prádanos, *Chem. Eng. Sci*., **65**(6), 2227 (2010).
52. K. M. Gheimasi, O. Bakhtiari and M. Ahmadi, *Chem. Eng. Res. Des*., **133**, 222 (2018).
53. Z. Noroozi and O. Bakhtiari, *Chem. Eng. Res. Des*., **152**, 149 (2019).
54. D. Dahlan, I. N. Marsih, I. Makertihartha, P. Praserthdam, J. Panpranot and I. Ismunandar, *Chem. Mater*., **2**, 31 (2012).
55. H. J. Kim, H. C. Lee, C. H. Rhee, S. H. Chung, H. C. Lee, K. H. Lee and J. S. Lee, *J. Am. Chem. Soc*., **125**(44), 13354 (2003).
56. A. A. Shamsabadi, F. Seidi, E. Salehi, M. Nozari, A. Rahimpour and M. Soroush, *J. Mater. Chem*., **5**(8), 4011 (2017).
57. S. Japip, H. Wang, Y. Xiao and T. S. Chung, *J. Membr. Sci*., **467**, 162 (2014).
58. H. Rabiee, A. Ghadimi and S. Abbasi, *Chem. Eng. Res. Des*., **98**, 96 (2015).
59. D.-Y. Peng and D. B. Robinson, *Ind. Eng. Chem. Fundam*., **15**(1), 59 (1976).
60. N. Azizi, T. Mohammadi and R. M. Behbahani, *J. Energy Chem*., **26**, 454 (2016).
61. D. M. Ruthven, *Principles of adsorption and adsorption processes*, Wiley, America (1984).
62. H. Rabiee, S. M. Alsadat, M. Soltanieh, S. A. Mousavi and A. Ghadimi, *J. Ind. Eng. Chem*., **27**, 223 (2015).
63. A. D. Kiadehi, M. Jahanshahi, A. Rahimpour and S. A. A. Ghoreyshi, *Chem. Eng. Process*., **90**, 41 (2015).
64. C. Lu, J. Lv, L. Xu, X. Guo, W. Hou, Y. Hu and H. Huang, *Nanotechnology*, **20**(21), 215604 (2009).
65. H. R. Mahdavi, N. Azizi and T. Mohammadi, *J. Polym. Res*., **24**(5), 67 (2017).
66. D. Zhao, J. Ren, H. Li, X. Li and M. Deng, *J. Membr. Sci*., **467**, 41 (2014).
67. A. Ghadimi, M. Amirilargani, T. Mohammadi, N. Kasiri and B.

Sadatnia, *J. Membr. Sci.*, **458**, 14 (2014).
68. D. Zhao, J. Ren, H. Li, K. Hua and M. Deng, *J. Energy Chem.*, **23**(2), 227 (2014).
69. H. Wu, X. Li, Y. Li, S. Wang, R. Guo, Z. Jiang, C. Wu, Q. Xin and X. Lu, *J. Membr. Sci.*, **465**, 78 (2014).
70. B. Cheng, S. Qu, H. Zhou and Z. Wang, *J. Phys. Chem. B*, **110**(32), 15749 (2006).
71. H. J. Lee, S. H. Han and S. Y. Nam, *J. Membr. Sci.*, **485**, 10 (2015).
72. M. M. Rahman, V. Filiz, S. Shishatskiy, C. Abetz, S. Neumann, S. Bolmer, M. M. Khan and V. Abetz, *J. Membr. Sci.*, **437**, 286 (2013).
73. R. Abedini, M. Omidkhah and F. Dorosti, *RSC Adv.*, **4**(69), 36522 (2014).
74. O. G. Nik, B. Nohair and S. Kaliaguine, *Micropor. Mesopor. Mater.*, **143**(1), 221 (2011).
75. R. S. Murali, A. F. Ismail, M. A. Rahman and S. Sridhar, *Sep. Purif. Technol.*, **129**, 1 (2014).
76. M. Sadeghi, H. T. Afarani and Z. Tarashi, *Korean J. Chem. Eng.*, **32**(1), 97 (2015).
77. A. Mahmoudi, M. Asghari and V. Zargar, *J. Ind. Eng. Chem.*, **23**, 238 (2015).
78. A. Ghadimi, T. Mohammadi and N. Kasiri, *Int. J. Hydrogen Energy*, **40**(31), 9723 (2015).
79. R. Kesting, *J. Polym. Sci. Part C: Polym. Lett.*, **27**(6), 187 (1989).
80. M. Isanejad, N. Azizi and T. Mohammadi, *J. Appl. Polym. Sci.*, **134**, 44531 (2017).
81. J. K. Adewole, A. L. Ahmad, S. Ismail, C. P. Leo and A. S. Sultan, *J. Appl. Polym. Sci.*, **132**, 42205 (2015).
82. M. Iqbal, Z. Man, H. Mukhtar and B. K. Dutta, *J. Membr. Sci.*, **318**(1-2), 167 (2008).
83. M. Rezakazemi, A. E. Amooghin, M. M. Montazer-Rahmati, A. F. Ismail and T. Matsuura, *Prog. Polym. Sci.*, **39**(5), 817 (2014).
84. M. Mohagheghian, M. Sadeghi, M. P. Chenar and M. Naghsh, *Korean J. Chem. Eng.*, **31**(11), 2041 (2014).
85. D. Roilo, P. N. Patil, R. S. Brusa, A. Miotello, S. Aghion, R. Ferragut and R. Checchetto, *Polymer*, **121**, 17 (2017).
86. M. Aroon, A. Ismail, T. Matsuura and M. Montazer-Rahmati, *Sep. Purif. Technol.*, **75**(3), 229 (2010).
87. A. Car, C. Stropnik, W. Yave and K.-V. Peinemann, *J. Membr. Sci.*, **307**(1), 88 (2008).
88. W. Yave, A. Car, K.-V. Peinemann, M. Q. Shaikh, K. Rätzke and F. Faupel, *J. Membr. Sci.*, **339**(1-2), 177 (2009).
89. N. Azizi, T. Mohammadi and R. M. Behbahani, *J. Nat. Gas. Sci. Eng.*, **37**, 39 (2017).
90. P. Bernardo, J. C. Jansen, F. Bazzarelli, F. Tasselli, A. Fuoco, K. Friess, P. Izák, V. Jarmarová, M. Kačírková and G. Clarizia, *Sep. Purif. Technol.*, **97**, 73 (2012).
91. L. Dong, M. Chen, J. Li, D. Shi, W. Dong, X. Li and Y. Bai, *J. Membr. Sci.*, **520**, 801 (2016).